# Rectified Flow over an Elongated Topographic Feature along a Vertical Wall

JACQUES VERRON,* DOMINIQUE RENOUARD,* DON L. BOYER,† GABRIEL CHABERT D'HIERES,* THONG NGUYEN,* AND HENRI DIDELLE*

*Laboratoire des Ecoulements Géophysiques et Industriels, Institut de Mécanique de Grenoble, Grenoble, France
†College of Engineering and Applied Sciences, Environmental Fluid Dynamics Program and Department of Mechanical and Aerospace Engineering, Arizona State University, Tempe, Arizona

(Manuscript received 22 March 1994, in final form 14 September 1994)

ABSTRACT

Alongshore oscillatory flows over an elongated topographic feature next to a vertical wall for a homogeneous, rotating fluid were investigated by means of numerical and laboratory experiments. The physical experiments were conducted in the Grenoble 13-m diameter rotating tank, in which an elongated obstacle of limited longitudinal extent was placed along the vertical sidewall. The background oscillating motion was obtained by periodically varying the platform angular velocity. Fluid motions were visualized and quantified by direct velocity measurements and particle tracking. The numerical model employed was a tridimensional model developed by Haidvogel et al. It consists of the traditional primitive equations, that is, the Navier–Stokes equations for a rotating fluid with the addition of the hydrostatic, Boussinesq, and incompressibility approximations. (The experiments described here employ the homogeneous version.) The numerical formulation uses finite differences in the horizontal and spectral representation in the vertical dimensions.

Both the laboratory and numerical experiments show that in the range of dimensionless parameters considered, two distinct flow regimes, based on general properties of the rectified flow patterns observed, can be defined. It is further shown that the flow regime designation depends principally on the magnitude of the temporal Rossby number, $Ro_t$, defined as the ratio of the flow oscillation to the background rotation frequency. Good qualitative and quantitative agreement is found between the laboratory experiments and the numerical model for such observables as the spatial distribution of rectified flow patterns. Several other flow observables are defined and their relation with the system parameters delineated.

## 1. Introduction

The nonlinear generation of a mean flow by oscillatory or other unsteady currents or turbulence (i.e., rectification) is for the most part studied in relation to the ubiquitous presence of tides. Such rectification processes have been observed in numerous places, for instance along the Georges Bank (Butman et al. 1982; Tee 1985), where measurements clearly suggest an anticyclonic mean circulation around the Georges Bank with the principal currents being along isobaths, and the rectified flow being depth dependent. Garreau and Mazé (1991) made similar observations of rectification of tidal motion in the vicinity of the La Chapelle Bank (47°30′N, 7°30′W), where the principal dynamical feature is a semidiurnal tide, the maximum speed of which near the 200-m isobath is $\approx 0.3$ m s$^{-1}$ during neap tide and $\approx 0.7$ m s$^{-1}$ at spring tide; the measurements indicate that the mean current along the 200-m contour can reach 10%–20% of the tidal amplitude and that there is vertical dependence as well as the existence of substantial cross-isobath transport. There are also observations of rectified flows around Bermuda (Stommel 1954), Fieberling Guyot in the North Pacific (Genin et al. 1989; Eriksen 1991) in the Bay of Biscay (Pingree and Le Cann 1990), in the Straits of Dover (Brylinski and Lagadeuc 1990), and the North Sea (Maas 1987; Maas and Van Haren 1987). Rectification may also be driven by a complete spectrum of motions as discussed by Holloway (1987). This may include, for example, long and short periods of wind forcing (Haidvogel and Brink 1986).

One significant feature is that, irrespective of the direction of the incident, unsteady, forcing flow, the local, mean, rectified flow is in a direction such that the shallow water is on the right, facing downstream (in the Northern Hemisphere). In the case of a simple slope, the topographically equivalent $\beta$ effect will therefore induce a rectified "westward-equivalent" current. The amplitude of this rectified flow can be a significant fraction of the amplitude of the forcing flow, for example, a significant fraction of the amplitude of tidal currents. Consequently, rectification can contribute significantly to mean current systems in the vicinity

*Corresponding author address:* Dr. Jacques Verron, Institut de Mécanique Grenoble, LEGI/BP 53X, 38041 Grenoble, Cedex, France.
E-mail: verron@img.fr

of the shelf break and, by extension, to the structure of the coastal current system itself. An interesting and unique result of the present experiments is that a flow regime is found ("bank" flow regime) such that, for a portion of the rectified flow, the coast is on the left facing downstream (see below).

In the context of tides, Robinson (1981) described three possible generation mechanisms for a rectified flow: (i) the change in relative vorticity necessary for the conservation of potential vorticity, (ii) the generation of vorticity when there is lateral shear in a flow, even when the depth is uniform, and (iii) the generation of vorticity due to the shear in the depth-distributed friction force when there is a depth variation in a direction normal to the local velocity. The second mechanism appears only if one adopts a quadratic representation of the bottom friction. Note that depth variation alone may be sufficient to support rectification. Zimmerman (1978) derived the applicable vorticity equation depending on the presence of depth variations and Coriolis and viscous effects, referring to them as the Coriolis and frictional torques, respectively. For rectification, both mechanisms require a phase shift between the vorticity field and the background tidal current.

Among the theoretical studies employing these mechanisms for depth-independent models are those of Huthnance (1973, 1981), Zimmerman (1978, 1980), Tee (1979, 1980), Yang and Tee (1987), Loder (1980), and Loder and Wright (1985). Maas and Zimmerman (1989a,b) have developed a numerical model for oscillatory, stratified flow normal to shelf breaks with infinitesimal step size $h/H \ll 1$, where $h$ is the height of the shelf and $H$ the depth of the deep ocean. Their resulting along- and cross-isobath residual and tidal circulations and isopycnal elevations have a well-defined localized structure in the cross-isobath vertical plane. More recently, Chen (1992) considered numerically the tidal rectification of a stratified ocean in the vicinity of two-dimensional model topography, including a model for Georges Bank. For a barotropic tidal current normal to a two-dimensional topography, the results suggest a balance between Coriolis effects and nonlinear advection in the cross-isobath direction and between viscous forces and nonlinear advection in the along-isobath direction. Chen (1992) also suggests that stratification may play a significant role in the spatial structure of the rectified currents. Garreau and Mazé (1991) developed an interpretative model for their observations near La Chapelle Bank in which they indicated that the nonlinear dynamics of an inviscid ocean can act as a flow rectification mechanism.

Motivated by field observations in the vicinity of Fieberling Guyot, Boyer et al. (1991, hereafter B91) studied the oscillatory motion of a homogeneous, rotating fluid in the vicinity of an isolated topographic feature, both in the laboratory and numerically. The experiments clearly showed that a mean anticyclonic vortex is formed above the topographic feature and that the spatial and temporal Rossby numbers of the background flow are key parameters for determining the typical trajectories. This analysis was extended to stratified oscillating flows (Boyer and Zhang 1990a,b; Zhang and Boyer 1993) and to multiple seamounts (Zhang and Boyer 1991). Also related to the present study is the analysis of the rectified flow along a vertical coastline. The driving mechanism in this case is a nonlinear coupling between the vertical shear layers, bottom Ekman layers, and oscillating free stream (Chabert d'Hières 1991; Zhang et al. 1993, 1994).

The purpose of the present study is to explore the flow characteristics, including rectified currents, resulting from a homogeneous, zero-mean, oscillatory motion past a topographic feature located along a lateral boundary in the presence of background rotation. The work is viewed as a natural extension of the B91 study of oscillatory flow past an isolated feature located far from lateral boundary surfaces. The emphasis is on obtaining a better understanding of the motion fields produced by the interaction of oscillatory background motions with idealized topography. Both numerical and laboratory approaches are used so that intercomparisons can lead to a deeper understanding of the physical processes involved.

The layout of the paper is as follows. In section 2, the physical system and the parameters of the problem, as well as the experimental facility and the techniques used are discussed. Section 3 briefly presents the numerical model. In section 4, the results obtained, such as the measured rectified current, and the flow regimes are presented. Finally, in section 5 these results are discussed with regard to the role played by the bathymetry.

## 2. Physical system, experimental setup, and techniques

This article considers the interaction of an oscillating, alongshore current with an elongated topographic feature located along a vertical sidewall; see Figs. 1a,b. The same model was used for both the laboratory and numerical experiments.

A layer of homogeneous fluid is confined by a rectilinear wall. The depth of this layer is $H$. The system rotates about a vertical axis with an angular velocity $\Omega$. (Coriolis parameter $f = 2\Omega$.) A bank, whose maximum height is $h_0$, is placed along the wall. The horizontal direction along the coast is denoted as $x$, $y$ is the direction normal to the coast, while $z$ is vertically upward. The origin of this Cartesian coordinate system is at the free surface along the coast (wall), at the center of the topographic feature. In the midtransverse section, the height of the bank is defined as

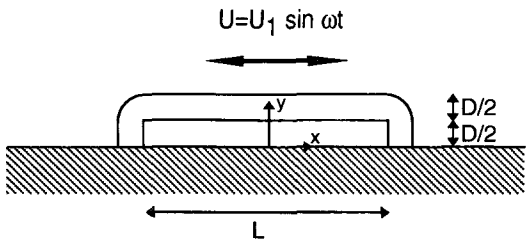


a

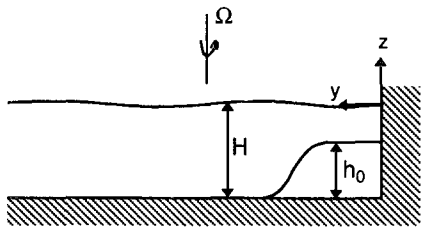


b

FIG. 1. (a) Plan view and (b) vertical section of the model system, and (c) its implementation in the laboratory. (d) Plan view of the computational domain.

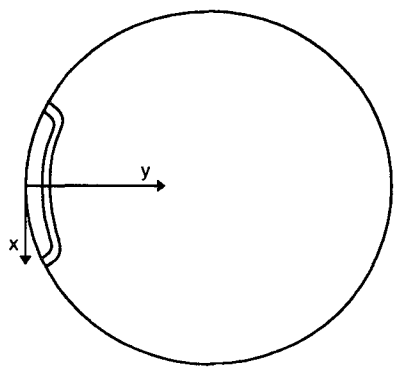


c

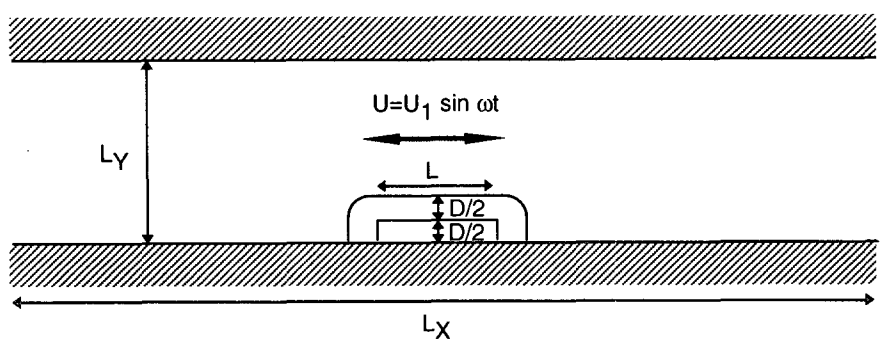


d

$$h = \begin{cases} h_0, & 0 < y < D/2 \\ h_0\left[\cos\dfrac{\pi(y - D/2)}{D}\right]^2, & D/2 < y < D \\ 0, & y > D. \end{cases} \quad (1)$$

Relation (1) describes the profile for a vertical section at all locations along the perimeter of the bank. The characteristic alongshore dimension, $L$, is defined as the length of the flat plateau along the coast. An oscillatory current is flowing in the direction parallel to the coast and is defined by

$$U = U_1 \sin(\omega t),$$

where $U_1$ and $\omega$ are the amplitude (uniform in space) and the frequency of the current. The mean forcing velocity during one-half cycle of the flow oscillation

$$\bar{U}_1 = \frac{2}{\pi} U_1$$

is taken to be the characteristic velocity scale. The width of the bank, $D$, is chosen as the characteristic lateral length scale. For the purposes of laboratory convenience, the configuration of Figs. 1a,b must be adapted to a circular geometry, see Fig. 1c. The numerics, for their part, are adapted to a channel geometry as in Fig. 1d, where $L_X$ and $L_Y$ are the channel length and width, respectively.

It is convenient to characterize the system by the following nondimensional parameters:

$$\mathrm{Ro} = \frac{\bar{U}_1}{fD} \quad \text{(spatial) Rossby number,}$$

$$\mathrm{Ro}_t = \frac{\omega}{f} \quad \text{temporal Rossby number,}$$

$$\left.\begin{aligned} E_h &= \frac{A_h}{fD^2} \\ E_v &= \frac{A_v}{fH^2} \end{aligned}\right\} \text{horizontal and vertical Ekman numbers,}$$

$$\mathrm{Fr} = \frac{f^2 D^2}{gH} \quad \text{Froude number,}$$

as well as by the aspect ratios $H/D$, $h_0/D$, and $L/D$. Here $A_h$ and $A_v$ are assumed to be constant eddy viscosity coefficients in the horizontal and vertical dimensions, respectively. In the laboratory, $A_h$ and $A_v$ are taken to be as the kinematic viscosity $\nu$, and $g$ is the gravitational acceleration. Note that the Reynolds number can be expressed from the previous numbers as $\mathrm{Re} = \bar{U}_1 D/A_h = \mathrm{Ro}/E_h$. It is also convenient to define $X$ as the normalized distance traveled by an undisturbed fluid parcel in one-half of a flow cycle:

$$X = \frac{\pi \bar{U}_1}{\omega D} = \pi \frac{\mathrm{Ro}}{\mathrm{Ro}_t}.$$

The laboratory experiments were carried out on the large rotating table at the Institut de Mécanique de Grenoble. This 14-m diameter rotating platform is equipped with a 13-m diameter, 1.2-m deep cylindrical tank. The obstacle is placed along the wall. Its shape is defined by (1) with $D = 1$ m, $L = 5$ m, and $h = 0.3$ m (Fig. 1). The tank is filled with fresh water, the total fluid depth of which is $H = 0.35$ m. The background flow is established by oscillating the platform with an angular rotation $\Omega$ given by

$$\Omega = \Omega_0 + \Omega_1 \sin(\omega t),$$

with $\Omega_0 = 0.125\ \mathrm{s}^{-1}$ and $\Omega_1 \ll \Omega_0$. Such a system is dynamically equivalent to a current fluctuating over a fixed bottom.

Because $\Omega_1 \ll \Omega_0$, the Coriolis parameter $f$ can be considered as constant and equal to $f = 0.25\ \mathrm{s}^{-1}$. The inertial period is therefore 25 s and the background rotation period $2\pi/\Omega_0$ is 50 s. Thus, we are simulating an oscillatory movement parallel to a coast. The tangential velocity at $r = 6$ m is chosen as the reference velocity, $U_1 = \Omega_1 r$, and then used to define the mean forcing velocity $\bar{U}_1$. The geometrical parameters and the Ekman number are constant in the experiments. The only varied parameters are thus Ro and $\mathrm{Ro}_t$.

Table 1 shows typical values for the dimensional and nondimensional parameters for the models as well as for some actual oceanic situations. Although the physical and model system does not aim at precisely modeling some region of the real ocean, it is clearly expected to shed some light on mechanisms that could be encountered in nature. In the ocean, at the scale of shelf breaks, $D$ is typically 50 km and a typical topographic jump from 200 m on the plateau to about 4000 m in the abyssal plain will correspond to a slope of approximately 10%. In the laboratory, the topographic slope may be exaggerated because $H/D$ is not a similarity

TABLE 1. Flow parameters.

| | Oceanic shelf break | Laboratory experiment | Numerical experiment |
|---|---|---|---|
| Dimensional | | | |
| $f$ | $10^{-4}\ \mathrm{s}^{-1}$ | $0.25\ \mathrm{s}^{-1}$ | $0.25\ \mathrm{s}^{-1}$ |
| $D$ | 50 km | 1 m | 1 m |
| $H$ | 4000 m | 0.35 m | 0.35 m |
| $h_0$ | 3800 m | 0.30 m | 0.30 m |
| $U$ | $0.1\ \mathrm{m\ s}^{-1}$ | $0.01\ \mathrm{m\ s}^{-1}$ | $0.01\ \mathrm{m\ s}^{-1}$ |
| $A_h$ | $100\ \mathrm{m}^2\ \mathrm{s}^{-1}$ | — | $1.3 \times 10^{-4}\ \mathrm{m}^2\ \mathrm{s}^{-1}$ |
| $A_v$ | $10^{-4}\ \mathrm{m}^2\ \mathrm{s}^{-1}$ | — | 0 |
| $\nu$ | — | $10^{-6}\ \mathrm{m}^2\ \mathrm{s}^{-1}$ | — |
| Nondimensional | | | |
| Fr | $6 \times 10^{-4}$ | $2 \times 10^{-2}$ | $2 \times 10^{-2}$ |
| Ro* | $2 \times 10^{-2}$ | $4 \times 10^{-2}$ | $4 \times 10^{-2}$ |
| $E_h$ | $4 \times 10^{-4}$ | $4 \times 10^{-6}$ | $5.3 \times 10^{-4}$ |
| $E_v$ | $6 \times 10^{-8}$ | $3 \times 10^{-5}$ | 0 |

* Note that Ro was varied in the numerical experiments. The above figures are only indications of its typical value.

TABLE 2. Nondimensional parameters for the various experiments (numerical and laboratory) and corresponding dimensional parameters in the laboratory.

| Reference | Ro | $Ro_f$ | $X$ | $\Omega_1$ ($10^{-3}$ s$^{-1}$) | $\omega$ (s$^{-1}$) | $U_1$ ($10^{-2}$ m s$^{-1}$) | $\tau = 2\pi/\omega$ (s) |
|---|---|---|---|---|---|---|---|
| 1 | 0.041 | 0.40 | 0.32 | 2.67 | 0.10 | 1.6 | 62.8 |
| 2 | 0.041 | 0.60 | 0.22 | 2.67 | 0.15 | 1.6 | 41.9 |
| 3 | 0.041 | 0.80 | 0.16 | 2.67 | 0.20 | 1.6 | 31.4 |
| 4 | 0.041 | 1.20 | 0.11 | 2.67 | 0.30 | 1.6 | 20.9 |
| 5 | 0.081 | 0.60 | 0.43 | 5.33 | 0.15 | 3.2 | 41.9 |
| 6 | 0.081 | 0.80 | 0.32 | 5.33 | 0.20 | 3.2 | 31.4 |
| 7 | 0.081 | 1.20 | 0.21 | 5.33 | 0.30 | 3.2 | 20.9 |
| 8 | 0.081 | 1.59 | 0.16 | 5.33 | 0.40 | 3.2 | 15.7 |
| 9 | 0.122 | 0.60 | 0.64 | 8.00 | 0.15 | 4.8 | 41.9 |
| 10 | 0.122 | 0.80 | 0.48 | 8.00 | 0.20 | 4.8 | 31.4 |
| 11 | 0.122 | 1.20 | 0.32 | 8.00 | 0.30 | 4.8 | 20.9 |
| 12 | 0.122 | 1.59 | 0.24 | 8.00 | 0.40 | 4.8 | 15.7 |
| 13 | 0.127 | 0.16 | 2.50 | 8.33 | 0.040 | 5.0 | 157.0 |
| 14 | 0.139 | 0.22 | 2.00 | 9.17 | 0.055 | 5.5 | 114.0 |
| 15 | 0.134 | 0.28 | 1.50 | 8.75 | 0.070 | 5.3 | 90.0 |

parameter. The Froude number Fr $\ll 1$ supports the assumption that external gravity waves do not primarily affect the situation under investigation. Ekman numbers for the ocean are based on estimates for the turbulent viscosity coefficients of $A_h \approx 100$ m$^2$ s$^{-1}$ and $A_v \approx 10^{-4}$ m$^2$ s$^{-1}$ (Pedlosky 1979). In the laboratory experiments, both coefficients should be equal to the kinematic viscosity, $\nu$. It is noted that in both the ocean and the laboratory experiments, the Ekman numbers are small and thus viscous effects in the fluid interior, including the shelf slope region, should be small away from the lateral boundaries. As discussed by Pedlosky (1979), a scale for the relative thickness of the vertical Ekman layer is given by

$$\frac{\delta_v}{H} = E_v^{1/2}.$$

Regarding the effect of the sidewall, the same author proposes a scale for the lateral boundary layer thickness (Stewartson layer) as

$$\frac{\delta_h}{D} = \frac{E_h^{1/2}}{E_v^{1/4}}.$$

As estimated from the above relations, the sidewall boundary layer is expected to be significantly larger than its bottom counterpart; that is, $\delta_v \ll \delta_h$. It is clear, however, that in the vicinity of the coastline, the bottom Ekman layer will influence the nature of the flow in that region. Zhang et al. (1993, 1994) have investigated the rectification process for an oscillating alongshore current along a vertical wall in the presence of a flat bottom. This analysis applies in an approximate way far upstream and downstream of the topographic feature as well as along the coast in the vicinity of the plateau region. It was shown by laboratory and numerical experiments that a rectified flow does develop, with the coastline on its right, facing downstream, having a characteristic velocity scale $v_Z \sim \overline{U_1}$ and a characteristic lateral scale

$$\delta_Z \sim \left(\frac{\nu}{f}\right)^{1/2} \frac{\overline{U_1}}{\tilde{H}} \frac{\pi}{\omega},$$

where $\tilde{H}$ is the fluid depth in the vicinity of the coast. The largest lateral scale regarding such a layer would thus occur over the plateau region. For the experiments conducted in the present investigations, $\delta_Z/D < 0.08$. The scale of this layer is thus expected to be small and this confirms that friction is not anticipated to be of leading-order importance away from the coast.

Fifteen experiments were performed, the conditions of which are indicated in Table 2. In the laboratory, the reproducibility of the experimental procedure was checked by performing each set of experiments at least twice. The velocities in the tank were measured at six locations ($y$ = 0.25, 0.5, 0.65, 0.75, 0.85, and 1.1 m) along three radii, at $x = -1.5$, 0 and 1.5 m, at $z = -2.5$ cm below the free surface. Vertical velocity profiles were also determined for three experimental conditions. The velocities were measured by ultrasonic current meters. After the platform had oscillated for at least 10 oscillation periods in order for the system to spin up to a quasi-periodic state, data were recorded over five oscillation periods for one position of the current meters, and the meters were then rotated by 90° four times so as to eliminate possible drift. Straightforward, trigonometric relations yielded the $(u, v)$ velocity components. In addition, we recorded the trajectories of surface floats and used image processing to obtain an overall view of the characteristic flow patterns. Dye tracers were also used to visualize the fluid movements and check the general behavior recorded by the current meters and the floats.

The numerical model employed a channel domain with limited streamwise and cross-stream extent. The

channel dimensions were chosen so that neither the opposite wall nor the channel extremities significantly influenced the flow in the regions of interest. The parameters used, apart from viscosity, are identical to the ones in the laboratory experiments: $L = 5$ m, $D = 1$ m, $H = 0.35$ m, $h_0 = 0.30$ m, and $f = 0.25$ s$^{-1}$. The length of the channel $L_X$ is specified in such a way that the channel ends do not affect the flow field occurring within the bank region. In general, we choose $L_X = 20D$ (Fig. 1d). A width of $L_Y = 4D$ was found to be sufficient to ensure that the "deep ocean" sidewall did not perturb the flow in the vicinity of the topographic feature.

## 3. Numerical model

The numerical model used is the tridimensional primitive equation model introduced by Haidvogel et al. (1991) written in its channel configuration version. This model is based on the standard Navier–Stokes equations for a rotating fluid in which the hydrostatic, Boussinesq, and incompressibility approximations have been made. In addition, the rigid-lid approximation is assumed for filtering external gravity waves. This saves substantial amounts of computing time by permitting larger time steps. This approximation is justified by the smallness of the Froude number, Fr, as noted above. Note that while the rigid-lid approximation does not allow the free surface to slope, it can nevertheless accommodate pressure gradients, thus simulating a free-surface slope, in a particular cross stream.

The governing equations for a homogeneous fluid in the Cartesian coordinate system $(x, y, z)$ are

$$\frac{\partial u}{\partial t} + \mathbf{U}\cdot\nabla u - fv = -\frac{\partial \Phi}{\partial x} + \Gamma_x \tag{2a}$$

$$\frac{\partial v}{\partial t} + \mathbf{U}\cdot\nabla v + fu = -\frac{\partial \Phi}{\partial y} + \Gamma_y \tag{2b}$$

$$\frac{\partial \Phi}{\partial z} = -\frac{g}{\rho_0} \tag{2c}$$

$$\frac{\partial u}{\partial x} + \frac{\partial v}{\partial y} + \frac{\partial w}{\partial z} = 0, \tag{2d}$$

where $(u, v, w)$ are the components of the velocity $\mathbf{U}$, $f$ is the constant Coriolis parameter of the system, $\rho$ is the density, and $\Phi = p/\rho_0$ represents the dynamical pressure. The quantities $\Gamma_x$ and $\Gamma_y$ include both forcing and dissipation terms.

Equations (2a,b) are the horizontal momentum equations. Equation (2c) expresses the hydrostatic relation. The incompressibility assumption allows us to write the mass conservation equation (2d). Horizontal dissipation effects are modelled by a harmonic term for the inner fluid (Laplacian lateral friction). No dissipation effects were assumed at the bottom, thus reducing the system of equations to the familiar shallow-water equations. It would have been possible to model more or less accurately the Ekman bottom boundary layer by assuming some bottom friction parameterization. The drawback here would have been the requirement of fine vertical resolution. As discussed earlier, the scale of the bottom Ekman layer is expected to be rather small. Consequently, we made the assumption for this initial stage that bottom friction is not a fundamental mechanism in the rectification process. The a posteriori agreement between the laboratory and numerical results confirmed the validity of this hypothesis. Note that our strategy in using such a model was to capture the essential physics necessary for reproducing the basic laboratory phenomenon, but not to include all possible physical ingredients.

The set of equations (2) is solved using a finite-difference technique for the transformed, orthogonal, curvilinear coordinates in the horizontal plane. In the vertical plane, a $\sigma$-coordinate transformation, $\sigma = 1 + 2z/(H - h)$, is used. In the absence of bottom friction, the problem is reduced to solving for the depth-integrated flow over the vertical. A trapezoidal leapfrog time-stepping method is used for the temporal scheme.

Periodic boundary conditions are applied in the longitudinal direction of the channel. No-slip numerical boundary conditions are applied along the wall next to the bank. For simplicity, a slip condition is assumed on the opposite wall, which, in any case, has negligible influence on the flow over the bank. Note that keeping the slip boundary condition on the opposite wall avoids grid refinement in that region and the associated increase in computational cost.

The ability of the Haidvogel et al. (1991) model to handle a variable grid was used to refine resolution where needed. It is indeed useful to solve for the nonlinear interactions more precisely in regions where they are expected to be more active. This is the case along the vertical wall next to the bank and also over the steepest bank gradients. Resolution is therefore 7.6 mm ($D/13$) in the $x$ direction and 3 mm ($D/30$) in the $y$ direction over the topographic obstacle.

The lateral viscosity coefficient $A_h$ was chosen as $1.3 \times 10^{-4}$ m$^2$ s$^{-1}$ leading to a horizontal "numerical" Ekman number

$$E_h = \frac{A_h}{fD^2} = 5.3 \times 10^{-4}.$$

This choice results from a compromise between having the finest possible grid resolution (and the related smallest possible lateral viscosity required for numerical stability) and computational capabilities. This value, while significantly larger than the typical Ekman number for the laboratory, is considered as an acceptable order of magnitude for the ocean (Pedlosky 1979).

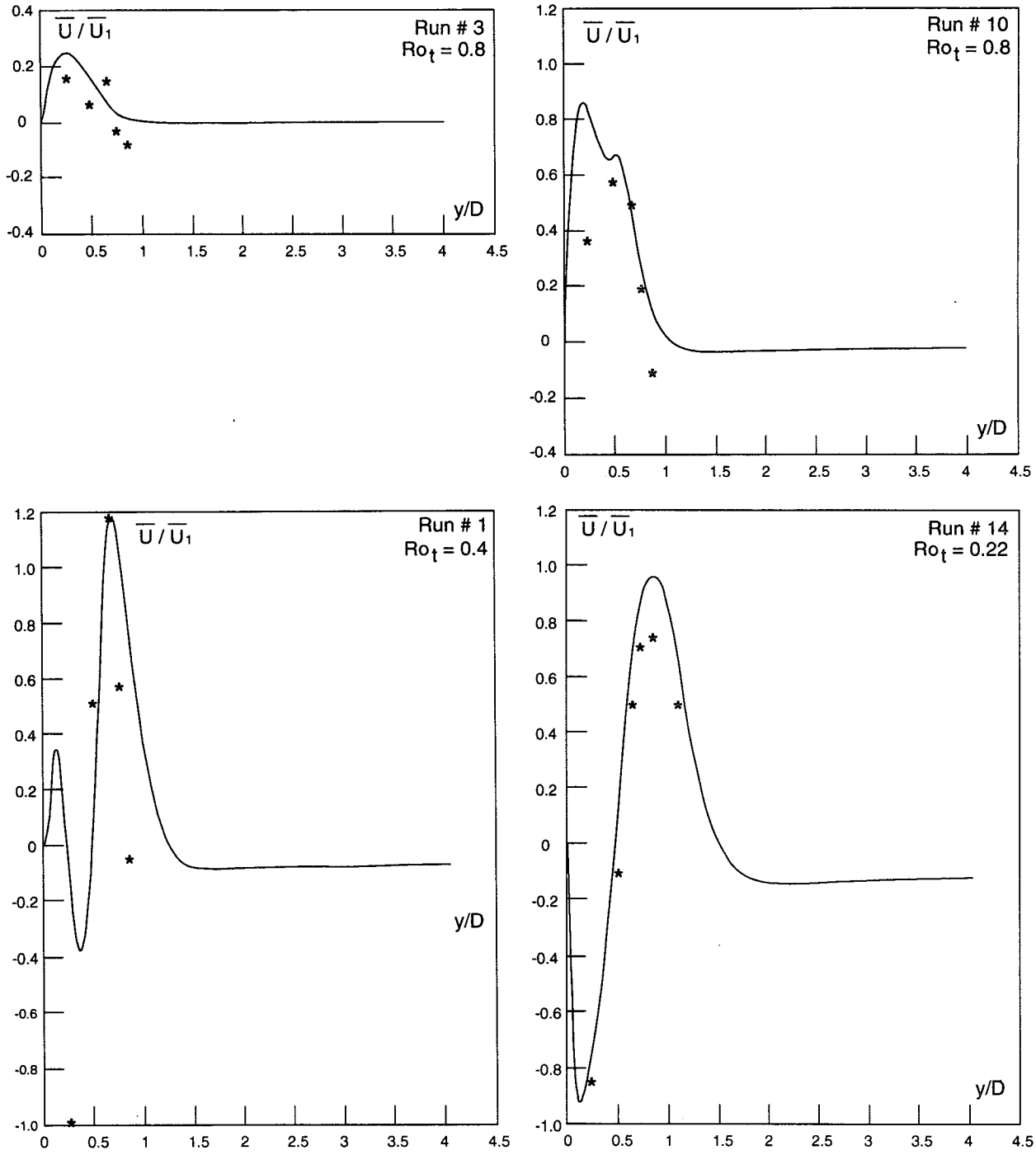


FIG. 2. Typical velocity profiles $\overline{U}/\overline{U_1}$ in the midsection. Runs (a) No. 3, (b) No. 10, (c) No. 1 and (d) No. 14. Computed values are shown by a solid line; laboratory measurements are indicated by stars.

## 4. Results

In analyzing the results, attention was directed mainly to characterizing the flow based on the general nature of the rectified currents. Comparisons between the laboratory flows and the numerical computations were made for the 15 experiments listed in Table 2.

It was found convenient first to define the various characteristic flows in terms of the midsection profiles of the streamwise rectified velocity component near the

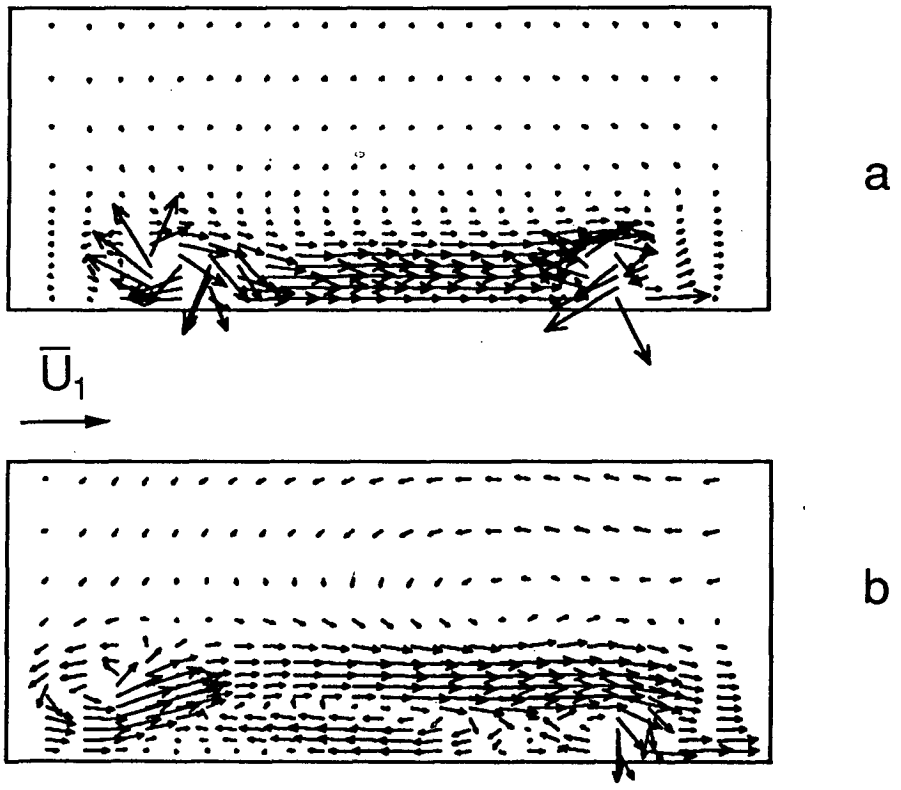


FIG. 3. Examples of model horizontal velocity fields in typical tips (Run No. 6) and bank (Run No. 13) flow regimes. (The actual computational domain is larger than the ones focused on here.)

free surface. Figures 2a–d show some examples for runs No. 3, 10, 1 and 14, respectively. These plots present the computed (solid line) and measured (stars) $u$ components of the normalized residual current $\overline{U}/\overline{U_1}$ along the midsection ($x = 0$), at $z = 2.5$ cm below the free surface. The scale is identical for all graphs. We note that, for the most part, there is good qualitative agreement between the numerical results and the laboratory experiments. It was observed that the dimensional rectified velocities measured in the laboratory may be very small; in run No. 3 for example, the maximum velocity is 1.6 mm $s^{-1}$. The following typical flow regimes were defined after examining the various profiles:

- *A "tips" flow regime.* This flow is characterized by (i) a broad rectified flow $U/\overline{U_1} < O(1)$ toward positive $x$ over the shelf and slope region (i.e., $0 < y/D < 1$) and (ii) a weak flow toward negative $x$ for $y/D > 1$; see Figs. 2a,b.
- *A "bank" flow regime.* This flow is characterized by (i) a rectified current toward negative $x$ over the plateau, (ii) a current toward positive $x$ near the slope and over the near deep ocean region, and (iii) a weak negative $x$ flow for $y/D > 1.5$; see Fig. 2d.
- *A transitional flow regime.* This flow is characterized along $y/D = 0$ by (i) a narrow rectified current toward positive $x$ along the coast, (ii) a narrow current toward negative $x$ on the plateau to the left of the shelf break, (iii) a strong flow toward positive $x$ over the slope region, and (iv) a weak negative $x$ flow for $y/D > 1$, see Fig. 2c. Along $y/D = 1.5$, the profile is the same as that along $y/D = 0$ for the bank flow regime, and along $y/D = -1.5$ it is the same as that corresponding to $y/D = 0$ for the tips flow regime.

Figures 3a–b are typical plots of the model, horizontal, rectified velocity field for the tips and bank flow regimes, respectively. Figure 3a for the tips regime (Run No. 6) shows that the rectified flow for the major portion of the ridge is unidirectional toward positive $x$, while strong anticyclonic eddy structures are located over the tips of the topography. In Fig. 3b for the bank flow regime (Run No. 13), on the other hand, the rectified flow shows a strong anticyclonic cell over the plateau and slope region, with cyclonic and anticyclonic eddy structures above the left and right tips of the topography, respectively. Similarly, Figs. 4a–c depict laboratory rectified velocity measurements at selected lateral positions for three streamwise locations. Figure 4a is an example of the tips flow regime (Run No. 6) while Fig. 4c illustrates a typical bank flow regime (Run No. 13). Figure 4b shows a transitional situation (Run No. 9) for which a residual anticyclone

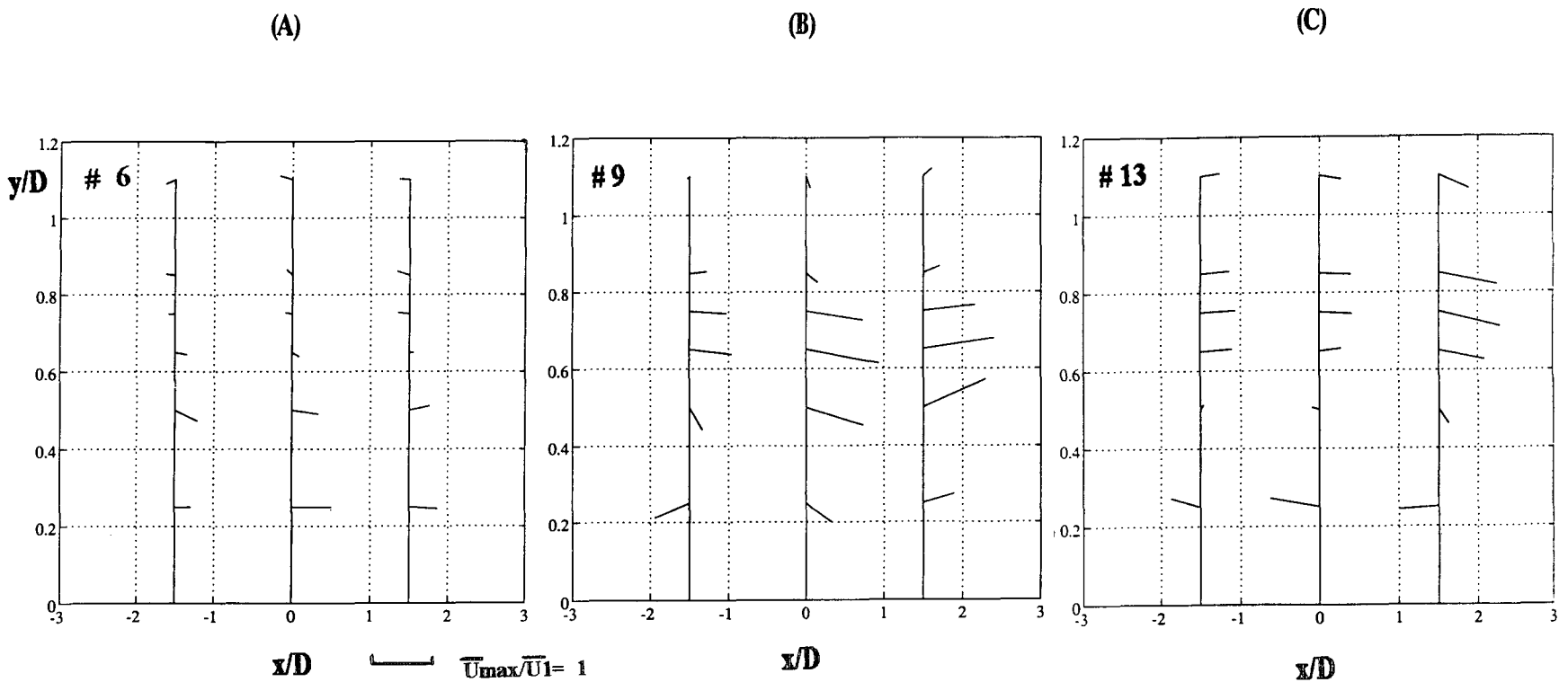


FIG. 4. Bar diagrams showing the horizontal velocity vectors of the surface rectified flow in the laboratory for (a) a tips flow regime (Run No. 6), (b) a transitional flow regime (Run No. 9), and (c) a bank flow regime (Run No. 13).

occurs over the upstream tip of the obstacle ($x/D = -1.5$) while a significant rectified flow is present over the slope.

Flow vertical structure was assessed in the laboratory by measuring the time-dependent horizontal velocity as a function of depth at selected locations. From this data, one can determine the vertical distribution of the horizontal rectified velocity. Figures 5a–b depict such measurements for two examples of the flow regime (Runs 3 and 9, respectively). Measurements are presented along $x = 0$, $y = 50$, 75, and 100 cm and for the depths indicated. The principal conclusion from Fig. 5 is that the rectified flow, to within experimental error, is roughly independent of height. This also validates the model approximation of a homogeneous vertical structure.

Hodographs for the time-dependent current can then be drawn from the same data by subtracting the residual current (Figs. 6a–b). Note that the $v$ component in these plots is indicated along the vertical with the $u$ component along the horizontal. The direction of the tip of the velocity vector is indicated by the arrows on the hodograph; the cycle begins at the symbol "○" and ends at "×." Figure 6a for Run No. 3 shows that the current turns anticyclonically along the vertical at the location $y = 100$ cm, while it turns cyclonically along $y = 50$ cm (edge of shelf). For Run No. 9 in Fig. 6b the current turns cyclonically in deep water and anticyclonically over the shelf. Over the slope, for both Runs No. 3 and 9, both cyclonic and anticyclonic current directions can be observed. At this stage we have no clear understanding of this rotational effect, which must be investigated further.

Surface float trajectories can be plotted from video tape recordings of the laboratory experiments. There is a striking difference in the general patterns of these Lagrangian views for the tips and the bank flow regimes. Figure 7a depicts trajectories of selected particles at various locations over the topography for a tips flow regime; the closed circle symbols denote the far rightward movement for each oscillation cycle. The floats exhibit small loops and a drift. The loops are anticyclonic over deep water and cyclonic over the shelf. The general mean drift of the floats is in accord with the rectified flow for tips flow regime experiments as discussed above and with the numerical experiments. Figure 7b shows trajectories for a typical bank flow regime experiment. In contrast to the tips regime, the trajectories are no longer small loops, but slightly oscillating trajectories almost parallel to the depth contours of the obstacle.

Figures 8a–d illustrate a series of complementary observations on the formation of large transient eddies, typical of the bank flow regime. They show a time sequence of photographs of a dye streak near the fluid surface that originated along a line parallel to the $y$ axis along $x = -3$ m at 30 s prior to the taking of photograph 9A (designated as $t = 0$ s) for Run No. 13. The dark "curved" line on each photograph is a line marked along $x = 0$ on the surface of the topography; the curvature is due to the fact that the line is drawn over a contoured bottom. Figure 8a is taken at a time for which the oscillatory current has reached its maximum leftward displacement and shows clearly the formation of a large cyclone along the left side ($x = -300$ cm) of the obstacle. Such a large cyclonic feature is formed by flow separation owing to the leftward (toward negative $x$) motion along the obstacle in the previous half-cycle. This cyclone is then advected to the right as shown in Figs. 8b–d by the rightward free-stream oscillating motion. The same process occurs 180° out of phase on the right side of the obstacle, but here an anticyclone is generated. This anticyclone is advected leftward over a much smaller distance along the obstacle than its cyclonic counterpart.

From video tapes of these eddy motions, it is possible to estimate the velocity of the cyclonic vortices generated along the left side of the obstacle as they move along the slope. In Run No. 13, shown in Fig. 8, for instance, its average velocity is $v \approx 7.2$ cm s$^{-1}$, whereas the maximum particle velocity along the radius $R = 5.5$ m is 4.6 cm s$^{-1}$; 5.5 m is roughly the radius along which the cyclone axis is moving. The cyclone thus moves about 1.5 times faster than the background maximum velocity of the flow. The occurrence of these large structures is also clearly visible from the current records at the stations at midbank along $x = 0$. Similar behavior was also observed in the numerical experiments.

Spectral analysis of the current component in such situations suggests an interpretation for the origin of these large eddies. The spectra of the velocity records distinctly show that for the bank flow regime experiments there are large second, third, and fourth harmonics of the oscillatory motion. For instance, in Run No. 13, there is a clear signal for $t = 31$ s, both on the $u$ and $v$ components of the current records. Now computing the wavelength of a continental Rossby wave with such a period (Pedlosky 1979), we find $l = 2.3$ m, which is close to the oscillating excursion for that run (2.5 m); thus in that particular instance the oscillatory movement probably forced a continental Rossby wave, the wavelength of which was half the obstacle length.

## 5. Discussion

First and foremost, we see that, considering the complexity of the physical system addressed and the simplification used in the numerical model, there is fairly good agreement between the laboratory and numerical experiments. The study raises the consideration of the origin of the rectified current. The possible mechanisms for flow rectification are the effect of the bathymetric variation and the frictional effects. It will be recalled that bottom friction was neglected in the numerical

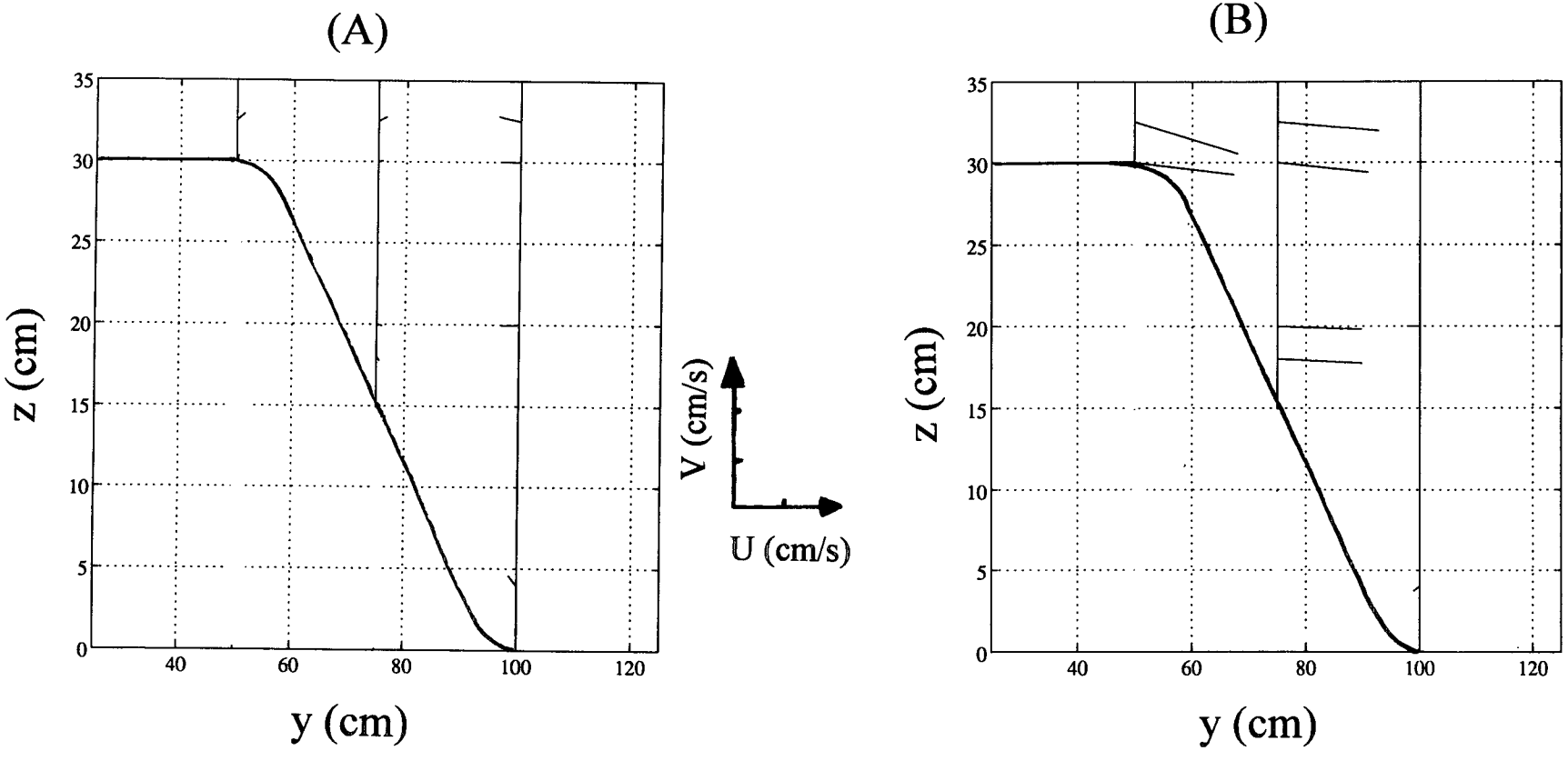


FIG. 5. Bar diagram of the residual current in the laboratory at various depths ($z$ = 2.5, 5, 15, 17, or 31 cm from the free surface), at three locations ($y$ = 50, 75, and 100 cm from the sidewall), along the line $x$ = 0 for Runs No. 3 (A) and No. 9 (B).

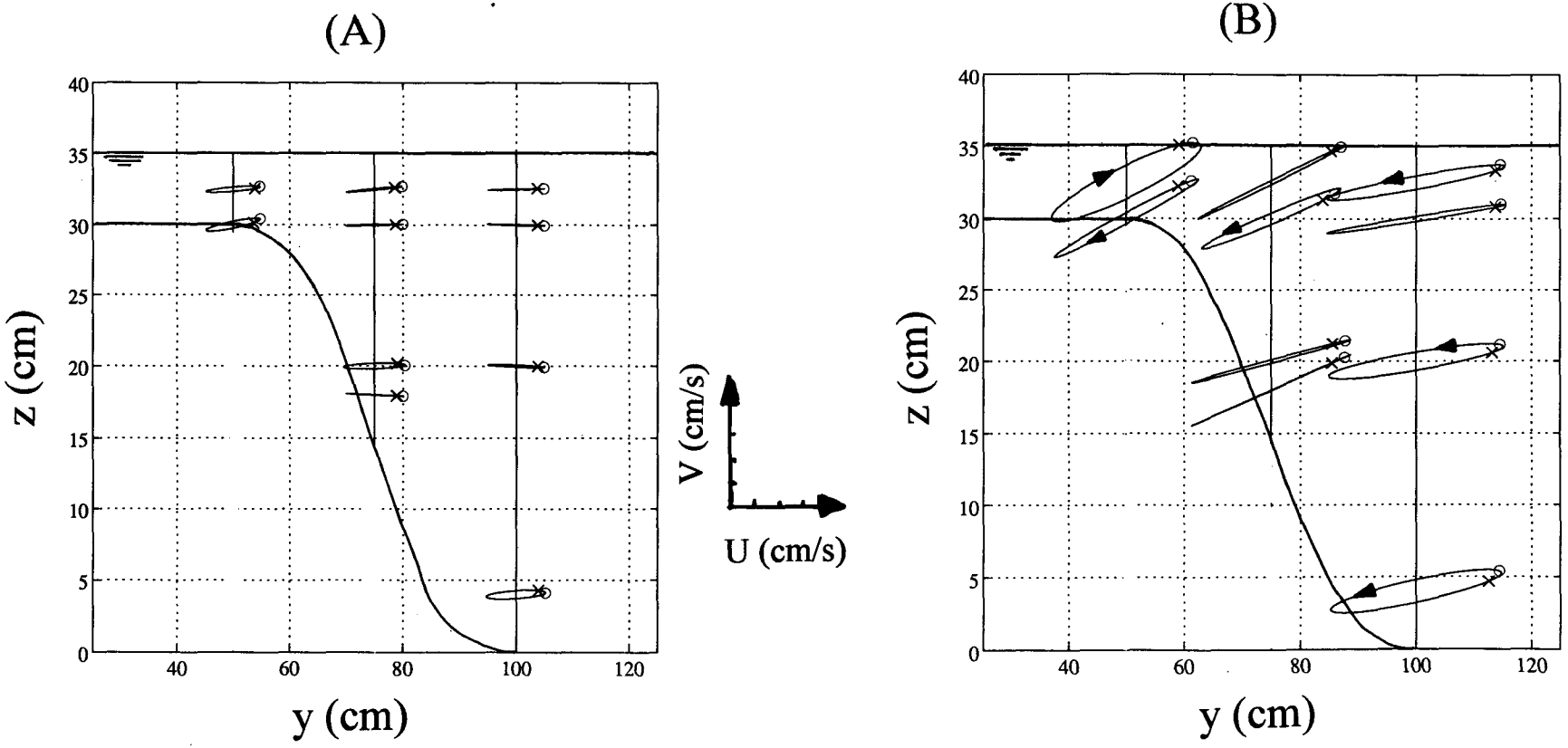


FIG. 6. Tidal ellipses (hodographs) of the main current in the laboratory at various depths ($z$ = 2.5, 5, 15, 17, or 31 cm from the free surface), at three locations ($y$ = 50, 75, and 100 cm from the sidewall) along the line $x$ = 0 for Runs No. 3 (A) and No. 9 (B).

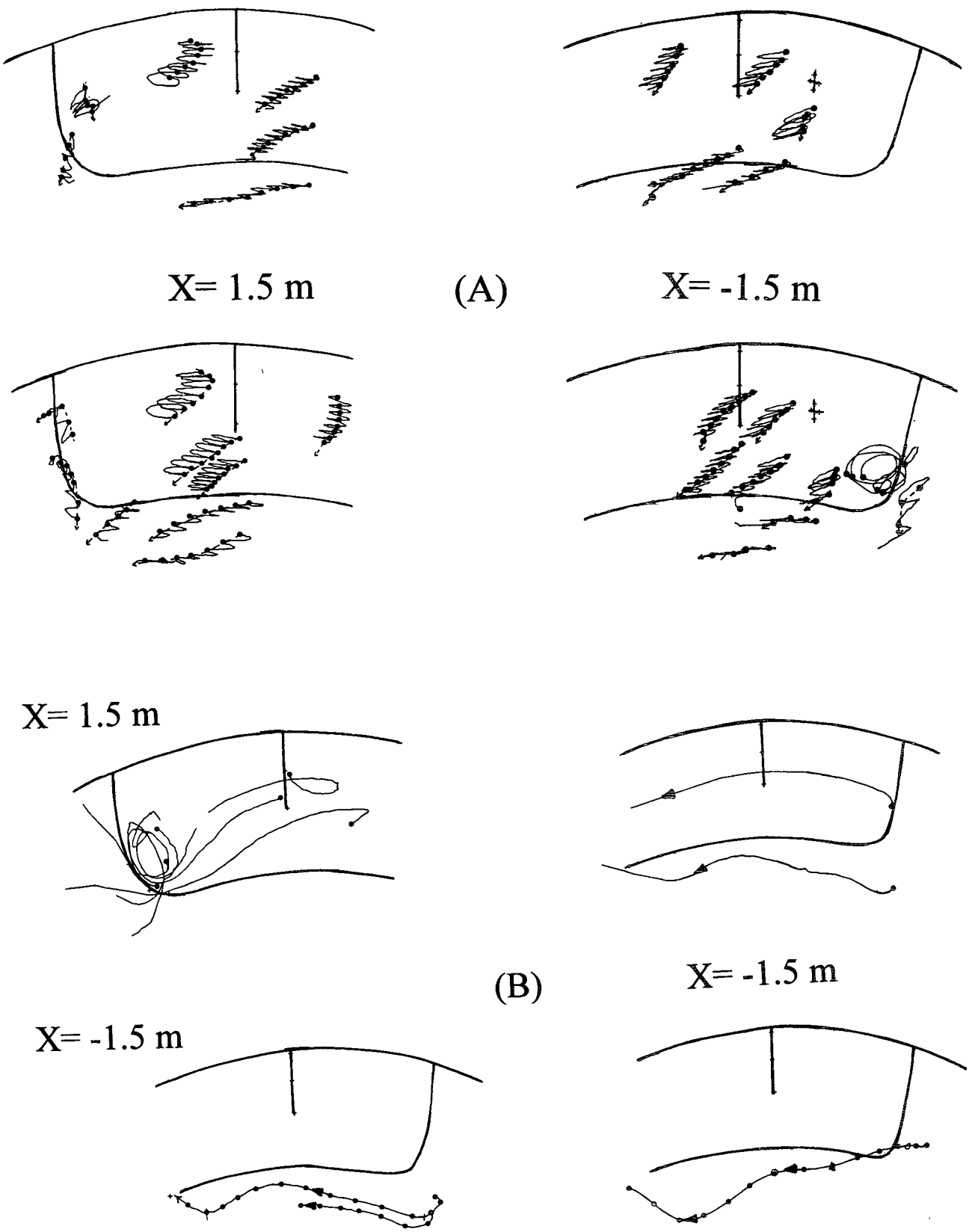


FIG. 7. Examples of float trajectories for Runs No. 3 (A) and No. 13 (B).

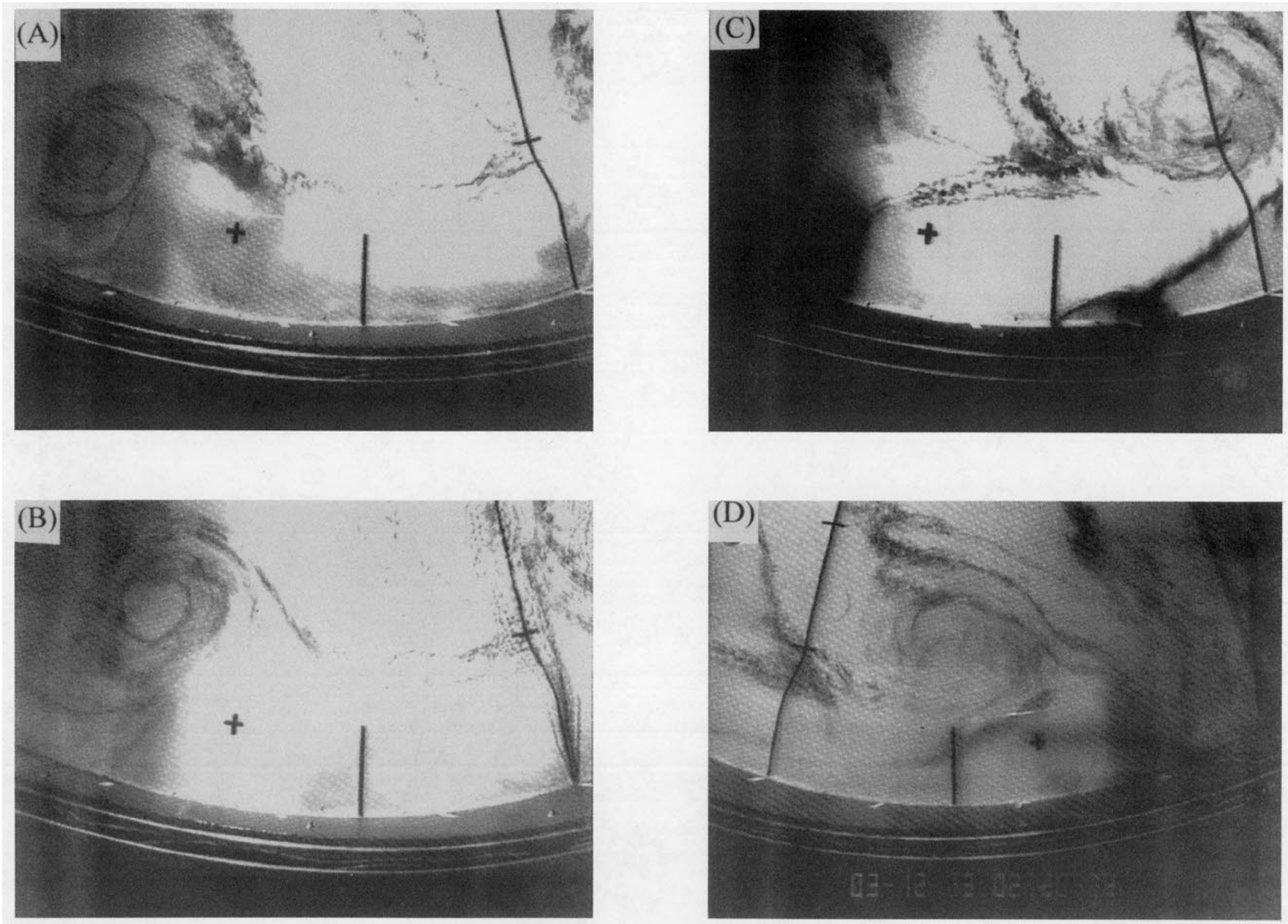


FIG. 8. Top view photographs showing the drift of the cyclone generated periodically at the upstream (left) tip of the obstacle in Run No. 13. Times are 0 (A), 30 s (B, flow reversal), 63 s (C), and 81 s (D). In all pictures the long line corresponds to $x = 0$ (center of the obstacle), the shorter line to $x = -1.5$ m (A, B, C) or $x = 1.5$ m (D), and the crosses to $x = -2.5$ m, $y = 0.5$ m (A, B, C) or $x = 2.5$ m, $y = 0.5$ m (D).

model and thus that frictional effects enter the numerics only by lateral friction. The good agreement between the laboratory and numerical experiments suggest that bottom friction is thus proven not to be an essential ingredient of the rectification process observed in the laboratory. Moreover, scaling arguments led us to hypothesize that lateral friction is also not of leading-order importance away from the wall. Bathymetric variation alone would thus appear to be the main causal factor for the observed rectified currents.

In the literature on tidal vorticity, several authors (for example, Zimmerman 1978; Komen and Riepma 1981; Robinson 1981) have derived various forms of the shallow-water equations to express the production terms for a possible residual vorticity. As we mentioned in the introduction to the work by Robinson (1981), the first candidate mechanism for rectification results directly from the conservation of potential vorticity. In the case of significant bathymetric variation this production term may be important. In coastal regions and estuaries, the sea depth variation is usually small, meaning that dissipation processes, essentially bottom friction, are of prime importance. Here, we believe then that, in the same way than in the paper by B91, the production of relative vorticity induced by bathymetric change may account for most of the rectified current.

It is not our intention to rederive equations that are abundantly discussed in the literature. It is useful, however, to recall some findings of an analytical simplified approach to the elementary case of an inviscid flow. Starting from the familiar shallow-water equation written for the potential vorticity

$$\frac{D}{Dt}\left(\frac{\zeta + f}{H}\right) = 0$$

one can follow Zimmerman (1978) and derive a perturbation analysis around the oscillatory forcing flow $U$. The velocity and the vorticity are then written

$$v = U + u$$

$$\zeta = \Omega + \eta.$$

(Note that $\Omega$, the forcing flow vorticity, is zero in our particular case.) Assuming small perturbation velocities, it is classically found that the production of a perturbation vorticity $D\eta/Dt$ is associated with the term $f\mathbf{U}\cdot\nabla H/H$. More ample justifications for this calculation may be found in Zimmerman (1978) and Robinson (1981). This shows in particular that the production of a perturbation vorticity exists only if $\mathbf{U}$ is not normal to the topographic gradients. A scaling for the perturbation vorticity over an oscillation period $2\pi/\omega$ is given then by

$$\eta \sim \frac{fU_1 h}{\omega HD}.$$

We assumed here that the slope $h/D$ provides an order of magnitude for the topographic gradient. The perturbation vorticity may be related to the rectified current amplitude $V_R$ assuming, for example, a typical eddy size for the rectified current at the width scale, $D$, of the bank:

$$\eta \sim \frac{V_R}{D}.$$

This finally leads to a scale for the rectified current

$$\frac{V_R}{U_1} \sim \frac{f}{\omega}\cdot\frac{h}{H} \sim \mathrm{Ro}_t^{-1}\cdot\frac{h}{H}.$$

For a given geometry, the rectified flow amplitude is found to be controlled just by the amplitude of the temporal Rossby number. The numerous approximations required by this analytical approach and, in particular, the smallness of the perturbation velocity, limit its scope.

However, in the light of these analytical considerations, it is of particular interest to look at the maximum values of the rectified current in the different cases with respect to the nondimensional controlling parameters. Figure 9a shows a plot of the normalized maximum rectified current in the positive $x$ direction $\bar{U}_{\max}/\overline{U_1}$ as a function of $\mathrm{Ro}_t^{-1}$ for both the laboratory and the numerical experiments. Again good agreement is seen between the laboratory and the numerical results, although the latter are often larger. The data in Fig. 9a from this limited experimental program strongly suggest that the principal parameter determining the qualitative nature of the resulting flow fields is the temporal Rossby number, $\mathrm{Ro}_t$. Some of the data scatter is due to the fact that the observable $\bar{U}_{\max}/\overline{U_1}$ is also a function of Ro. Interestingly, it appears that the quantity $\bar{U}_{\max}/\overline{U_1}$ is maximum when $\mathrm{Ro}_t^{-1} \approx 1.7$; that is, when the forcing period is approximately twice the inertial period.

Figure 9b presents the same quantity $\bar{U}_{\max}/\overline{U_1}$ as a function of $X$, the normalized flow excursion during one-half of the oscillatory cycle. The data collapse is similar to that of Fig. 9a. Because $X \sim \mathrm{Ro}/\mathrm{Ro}_t$, this reinforces the fact that Ro is playing a limited role and provides additional support for the idea that the principal governing parameter is $\mathrm{Ro}_t^{-1}$. Figure 9b also reveals that the rectified velocity maximum occurs for $X \approx 0.5$, that is, when the flow excursion approximates the width of the slope region.

Two different types of behavior can further be identified on Figs. 9a and 9b: (i) a range for which the rectified velocity increases approximately linearly with $\mathrm{Ro}_t^{-1}$ and $X$ ($0 < \mathrm{Ro}_t^{-1} < 2$; $0 < X < 0.5$) and (ii) a range in which the velocity decreases with $\mathrm{Ro}_t^{-1}$ and $X$ ($\mathrm{Ro}_t^{-1} > 2$; $X > 0.5$). Within the range of parameters being investigated, the maximum velocity reached in the midsection is about $1.5\overline{U_1}$, which is approximately equal to $(\pi/2)\overline{U_1} = U_1$. No rectified flows exceeding

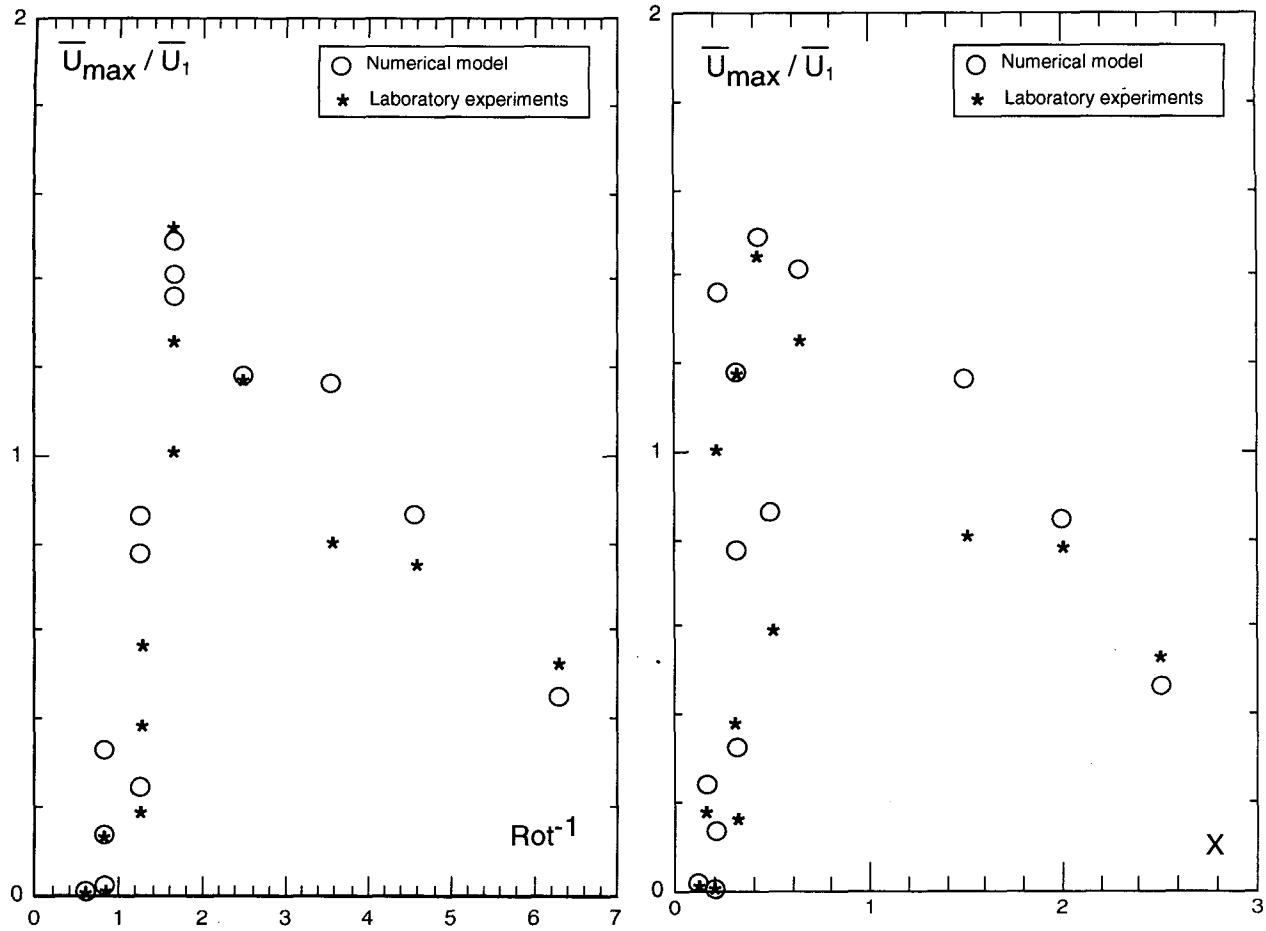


FIG. 9. Maximum rectified velocity in the midsection as a function of (a) $Ro_r^{-1}$ and (b) $X$.

$U_1$ were found in any of the experiments at any location. The maximum amplitude of the rectified flow seems therefore constrained in all cases by $\bar{U} < U_1$, that is, by the maximum amplitude of the incident forcing flow. Note that this maximum value is reached approximately at the transition point between the tips and bank flow regimes.

Using all these results it was possible to classify the experiments of Table 2 according to the previous general definitions to draw a flow regime diagram in ($Ro_r$, Ro) parameter space (Fig. 10). The respective run numbers are also indicated with reference to Table 2. This diagram clearly shows the dominance of $Ro_r$ in determining flow regimes.

Figure 11 summarizes the way in which maximum normalized rectified velocity $\bar{U}_{max}/\overline{U_1}$ in the midsection $x = 0$, varies in (Ro, $Ro_r$) parameter space. As in Fig. 9a, it shows that the rectified flow amplitude has a maximum for $Ro_r \approx 0.5$, that is, when the forcing flow oscillation is twice the inertial period.

Another distinction between the tips and the bank flow regimes appears that relates to the position of this maximum velocity. Figure 12 shows the normalized position of the maximum rectified velocity $d/D$ as a function of $Ro_r^{-1}$. Here $d$ is the distance from the coast. The velocity maximum clearly moves away from the coast as $Ro_r^{-1}$ increases; for small values of $Ro_r^{-1}$ the jet is located on the shelf whereas it shifts toward the slope region when $Ro_r^{-1}$ increases. The position computed agrees quite well with the observed jet location, granted that the distance between the probes does not allow for great precision in the measurement of $d$ in the laboratory. When $Ro_r^{-1}$ is large, the jet moves away from the shelf and there is a marked countercurrent that is maximum in the middle of the shelf; the numerical model exhibits the same behavior (see Fig. 2d). The marked data collapse again suggests that this observable $d/D$ depends primarily on a single parameter $Ro_r^{-1}$.

Although there are clearly two well-identified flow regimes, the observables exhibit a marked tendency to be organized under the control of the single parameter $Ro_r$. This is quite consistent with the simpler, analytical

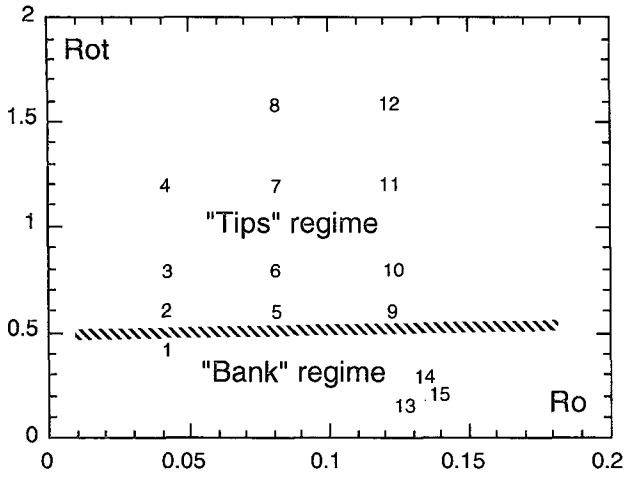


FIG. 10. Flow regime diagram in the (Ro, $Ro_t$) parameter space.

argument and reinforces the conjecture concerning the role of topography.

A number of other remarks may usefully be made about the so-called tips and bank flow regimes. As stated earlier, for the largest values of $Ro_t$, we observe the tips flow regime in which the rectified flow in the midbank portion is very weak. This is consistent with previous studies showing that rectification does not occur in the alongshore direction for an alongshore oscillatory current along a coastline of uniform cross section. In the absence of other mechanisms, such as nonlinear bottom friction, an infinite length obstacle like this will not give rise to any rectification (Haidvogel and Brink 1986). This result was checked numerically in the present case by extending the obstacle length $L$ to infinity. This can also be seen simply as a consequence of the previous analytical considerations, which suggest no rectification from an oscillatory flow parallel to the bank slope.

The basic rectification processes over the shelf break could therefore be interpreted as follows. The longitudinal variations of the transverse bathymetric gradients, where they exist (tips), suggest local rectification ($\mathbf{U}\cdot\nabla H \neq 0$) and, where they are absent (midbank slope) local rectification is also lacking ($\mathbf{U}\cdot\nabla H = 0$). Thus, when the flow excursion is at the scale of the tips ($X \sim D$), rectification stays confined to the tips and remains weak at midbank. For such cases, the tips flow regime is observed. When the flow excursion is at the scale of the characteristic streamwise length of the bank ($X \sim L$), the rectifying effects of the tips are sufficient for the whole bank to be taken over. The bank flow regime is then observed. In a word, one could say that longshore rectified currents are present only because the bank has tips.

As for the role of $Ro_t$, these mechanisms for the two observed regimes are compatible with what we would expect from topographic rectification at the different longitudinal scales $L$ and $D$. However, we must not rule out the influence of friction on the amplitude of the rectified flow, especially at large Rossby numbers. Further investigations into the complex role of the lateral and bottom boundary layers would be of great interest in this regard.

## 6. Summary and conclusions

The interaction between an alongshore oscillatory current and an elongated topographic feature placed along a vertical wall was investigated by means of laboratory and numerical experiments. The main conclusions focus on the intense rectified currents that are observed over the bank and along the coast. These rectified currents are mainly controlled by the topographic influences of the tips. The study has demonstrated the crucial role of the temporal Rossby number in determining the general nature of the characteristic flow patterns. For large $Ro_t$, one observes the tips regime in which the rectified flow over the midbank is unidirectional, but relatively weak. For small $Ro_t$, one obtains a relatively strong anticyclonic rectified flow pattern over the entire topographic feature; that is, the flow near the midbank has the coastline on the right over the shelf break, but reverses in direction near the coast.

The study has indicated the importance of alongshore variations in the shelf break geometry. It is expected that offshore canyons and ridges will strongly affect the rectification patterns resulting from alongshore oscillatory currents. The complex role of bottom and lateral boundary layers has not been investigated and is therefore not well understood at this time. The good agreement between the laboratory experiments and the numerical model in the present study, however, suggests that the present model is dominated by topographic effects and thus captures most of the physics

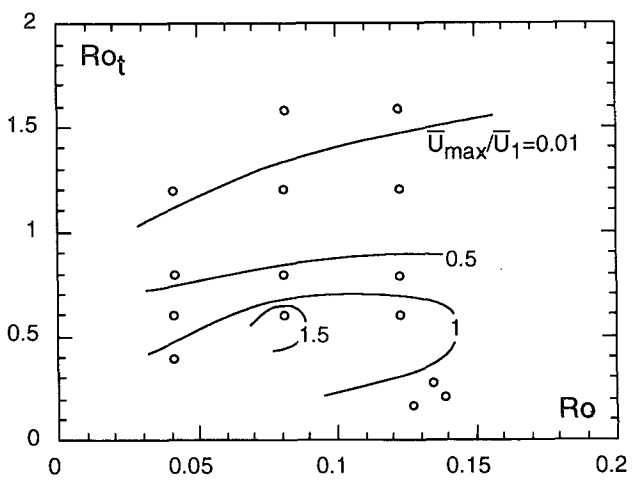


FIG. 11. Maximum rectified velocity in the midsection in the (Ro, $Ro_t$) parameter space.

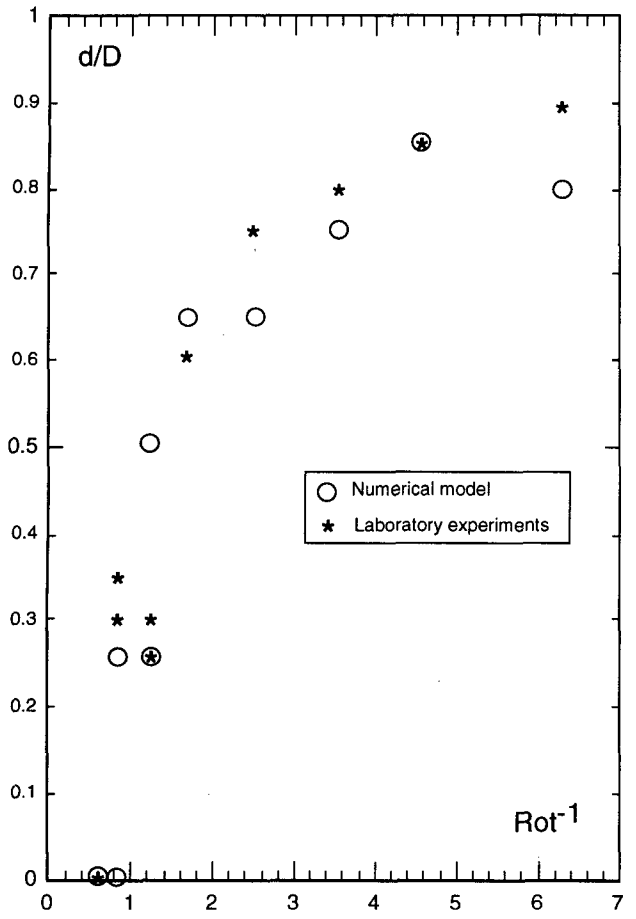


FIG. 12. Normalized distance to the coast, *d/D*, of the maximum velocity peak in the midsection of the bank versus $Ro_r^{-1}$.

involved in the rectification process. The present model has also neglected stratification effects that should be considered important in most oceanic applications. Although the present model is a crude one, it is suggested that the basic mechanism leading to flow rectification is representative of physical mechanisms at work in nature.

*Acknowledgments.* The authors are most grateful to R. Carcel who helped with the experiments and to J.-F. Revel, L. Pred'Homme, and S. Roque who did some of the data processing. This work was supported by CNRS-INSU. The calculations were made possible by the numerical facilities of the Centre de Calcul Vectoriel pour la Recherche in Palaiseau. Support of the Physical Oceanography Programs of the U.S. National Science Foundation (NSF) and the U.S.–France Program of NSF under Grants OCE-9301572 and INT-8820464 is also acknowledged.

## REFERENCES

Boyer, D. L., and X. Zhang, 1990a: The interaction of time-dependent rotating and stratified flow with isolated topography. *Dyn. Atmos. Oceans,* **14,** 543–575.

——, and ——, 1990b: Motion of oscillatory currents past isolated topography. *J. Phys. Oceanogr.,* **20,** 1425–1448.

——, G. Chabert d'Hières, H. Didelle, J. Verron, R. R. Chen, and L. Tao, 1991: Laboratory simulations of tidal rectification over seamounts: Homogeneous model. *J. Phys. Oceanogr.,* **21**(10), 1559–1579.

Brylinski, J. M., and Y. L. Lagadeuc, 1990: The inshore/offshore waters interface off the French coast in Dover Strait: A frontal area. *C.R. Acad. Sci. Paris,* t. **311,** Serie II, 535–540.

Butman, B., R. C. Beardsley, B. Magnell, D. Frye, J. A. Vermesch, R. Schlitz, R. Limeburner, W. R. Wright, and M. A. Noble, 1982: Recent observations of the mean circulation on Georges bank. *J. Phys. Oceanogr.,* **12,** 569–591.

Chabert d'Hières, G., 1992: Effects d'interaction entre le couche limite d'Ekman sous un écoulement de marée et la couche limite côtière. *Oceanol. Acta,* **SP 11,** 81–91.

Chen, C., 1992: Variability of current in Great South Channel and over Georges Bank: Observations and modelling. Ph.D. dissertation, Massachusetts Institute of Technology and Woods Hole Oceanographic Institution, 283 pp.

Ericksen, C., 1991: Observations of amplified flows atop a large seamount. *J. Geophys. Res.,* **96**(C8), 15 227–15 236.

Garreau, P., and R. Mazé, 1991: Tidal rectification and mass transport over a shelf break: A barotropic frictionless model. *J. Phys. Oceanogr.,* **22**(7), 719–731.

Genin, A., M. Noble, and P. F. Lonsdale, 1989: Tidal currents and anticyclonic motions on two North Pacific seamounts. *Deep-Sea Res.,* **36,** 1803–1816.

Haidvogel, D. B., and K. H. Brink, 1986: Mean currents driven by topographic drag over the continental shelf and slope. *J. Phys. Oceanogr.,* **16,** 2159–2171.

——, J. Wilkin, and R. Young, 1991: A semi-spectral primitive equation ocean circulation model using vertical sigma and orthogonal curvilinear horizontal coordinates. *J. Comput. Phys.,* **94,** 151–185.

Holloway, G., 1987: Systematic forcing of large scale geophysical flows by eddy-topography interaction. *J. Fluid Mech.,* **184,** 463–476.

Huthnance, J. M., 1973: Tidal current asymmetrics over the Norfolk Sandbanks. *Estuarine Coastal Mar. Sci.,* **1,** 89–99.

——, 1981: On mass transports generated by tides and long waves. *J. Fluid Mech.,* **102,** 367–387.,

Komen, G. J., and H. W. Riepma, 1981: Residual vorticity induced by the action of tidal currents in combination with bottom topography in the southern bight of the North Sea. *Geophys. Astrophys. Fluid Dyn.,* **18,** 93–110.

Loder, J. W., 1980: Topographic rectification of tidal currents on the sides of Georges Bank. *J. Phys. Oceanogr.,* **10,** 1399–1416.

——, and D. G. Wright, 1985: Tidal rectification and frontal circulation on the sides of Georges Bank. *J. Mar. Res.,* **43,** 581–604.

Maas, L. R. M., 1987: Tide-topography interactions in a stratified shelf sea. Ph.D. thesis, University Utrecht, 241 pp.

——, and J. J. M. van Haren, 1987: Observations on the vertical structures of tidal and inertial currents in the North Sea. *J. Mar. Res.,* **45,** 293–318.

——, and J. T. F. Zimmerman, 1989a: Tide-topography interactions in a stratified shelf sea. Part I: Basic equations for quasi-nonlinear internal tides. *Geophys. Astrophys. Fluid Dyn.,* **45,** 1–35.

——, and ——, 1989b: Tide-topography interactions in a stratified shelf sea. Part II: Bottom trapped internal tides and baroclinic residual currents. *Geophys. Astrophys. Fluid Dyn.,* **45,** 37–69.

Pedlosky, J., 1979: *Geophysical Fluid Dynamics.* Springer-Verlag, 624 pp.

——, and B. Le Cann, 1990: Structure, strength and seasonality of the slope currents in the vicinity of the Bay of Biscay region. *J. Mar. Biol. Assoc. U.K.,* **70,** 857–885.

Robinson, I. S., 1981: Tidal vorticity and residual circulation. *Deep-Sea Res.,* **28A**(3), 195–212.

Stommel, H., 1954: Serial observations of drift currents in the Central North Atlantic Ocean. *Tellus,* **6,** 204–214.

Tang, Y., and K. T. Tee, 1987: Effects of mean current interaction on the tidally induced residual current. *J. Phys. Oceanogr.,* **17,** 215–230.

Tee, K. T., 1979: The structure of three-dimensional tide generating currents. Part I: Oscillatory currents. *J. Phys. Oceanogr.,* **9,** 930–944.

——, 1980: The structure of three-dimensional tide generating currents. Part II: Residual currents. *J. Phys. Oceanogr.,* **10,** 2035–2057.

——, 1985: Depth-dependent studies of tidally induced residual currents on the sides of Georges Bank. *J. Phys. Oceanogr.,* **15,** 1818–1846.

Zhang, X., and D. L. Boyer, 1991: Current deflections in the vicinity of multiple seamounts. *J. Phys. Oceanogr.,* **21,** 1122–1138.

——, and ——, 1993: Laboratory study of rotating, stratified, oscillatory flow over a seamount. *J. Phys. Oceanogr.,* **23,** 1122–1141.

——, ——, G. Chabert d'Hières, D. Aelbrecht, and H. Didelle, 1993: Rectified flow along a vertical coastline. *Dyn. Atmos. Oceans,* **19,** 115–145.

——, ——, ——, and ——, 1994: Rectified flow of a rotating fluid along a vertical side wall. *Phys. Fluids,* **6**(4), 1440–1453.

Zimmerman, J. T. F., 1978: Topographic generation of residual circulation by oscillatory (tidal) currents. *Geophys. Astrophys. Fluid Dyn.,* **11,** 35–47.

——, 1980: Vorticity transfer by tidal currents over an irregular topography. *J. Mar. Res.,* **38,** 601–630.